Nuclear Instruments and Methods in Physics Research A 365 (1995) 446-461

NUCLEAR INSTRUMENTS & METHODS IN PHYSICS RESEARCH Section A

ELSEVIER

Detection efficiency of the neutron modular detector DEMON and related characteristics

I. Tilquin[a], Y. El Masri[a,*], M. Parlog[a,1], Ph. Collon[a], M. Hadri[a], Th. Keutgen[a,2], J. Lehmann[a], P. Leleux[a], P. Lipnik[a], A. Ninane[a], F. Hanappe[b], G. Bizard[c], D. Durand[c], P. Mosrin[c], J. Péter[c], R. Régimbart[c], B. Tamain[c]

[a] *Institut de Physique Nucléaire and FNRS, Université Catholique de Louvain, B-1348 Louvain-la-Neuve, Belgium*
[b] *Interactions Ion-Matière, CP 229, Université Libre de Bruxelles, B-1050 Bruxelles, Belgium*
[c] *Laboratoire de Physique Corpusculaire, IN2P3, CNRS/ISMRA, F-14050 Caen Cedex, France*

Received 19 December 1994; revised form received 30 March 1995

Abstract

DEMON is a detector array for neutrons emitted in heavy ion induced reactions at low to intermediate energies. The neutron detection efficiency of some single DEMON modules has been measured in the energy range 8–21 MeV, with detection thresholds down to 0.1 MeV equivalent-electron (MeVee). The influence on the efficiency of cross talk, neutron–gamma and neutron–charged particle discrimination techniques was found to be negligibly small. Monte Carlo simulations have been performed and are compared with the experimental data. The relative weight of the interaction channel $^{12}C(n,n'\gamma)$ in the organic liquid scintillator was determined experimentally. Taking into account observed saturation effects in the detector output, a calibration method is proposed for high light outputs, based on the energy loss of cosmic ray muons.

1. Introduction

DEMON (DEtecteur MOdulaire de Neutrons) is a Belgian–French[3] multidetector designed for the study of nuclear reaction-induced neutron emission. Various experiments have been and will be performed at heavy ion accelerators, such as CYCLONE at Louvain-la-Neuve (LLN), GANIL at Caen and VIVITRON at Strasbourg, at incident energies ranging from the Coulomb barrier up to 100 MeV per nucleon.

At each experimental site, DEMON will be installed in different configurations. At the Louvain-la-Neuve cyclotron facility the granularity and the packing fraction, into a large radius sphere (4π configuration), were chosen to provide reasonably good efficiency with minimum cross talk between adjacent modules. The angular acceptance of a single detector in the laboratory system is 5.2°. The neutron energy is determined by a time-of-flight technique and discrimination from γ-rays is achieved by pulse shape analysis. A subsequent, event-by-event, analysis is then used to define the neutron multiplicity distribution. These features make DEMON a versatile instrument for use in *low energy* nuclear physics. For example, one obtains an insight into the time scale and dynamics of the nuclear fission process, one can study nuclear viscosity, the mechanisms of complete and incomplete fusion and weakly bound neutron halo nuclei. In *intermediate energy* nuclear physics, DEMON will mainly be used to characterize the properties of normal and exotic hot nuclear matter.

DEMON is composed of 96 individual large volume cells for neutron detection and identification, which are assembled at the Louvain-la-Neuve cyclotron facility in a mosaic aluminium structure. The 4 m diameter sphere encircles the target chamber situated 5 m above ground, as shown in Fig. 1a. The total solid angle coverage is 5.02% of 4π. Each DEMON cell, a NE213 organic liquid scintillator coupled to a XP4512B photomultiplier (PM), allows neutron–gamma pulse shape discrimination. Twenty-four modules, normally placed in the forward cone, can also be equipped with charged particle rejection counters

* Corresponding author.

[1] On leave from the Institute of Atomic Physics of Bucharest, Romania.

[2] Supported by the Belgian IRSIA.

[3] Funded by the Belgian FNRS and French IN2P3 governmental institutions. The collaboration includes the Universities of Louvain and Brussels (Belgium), the CRN of Strasbourg and the LPC of Caen (France).

0168-9002/95/$09.50
SSDI 0168-9002(95)00425-4

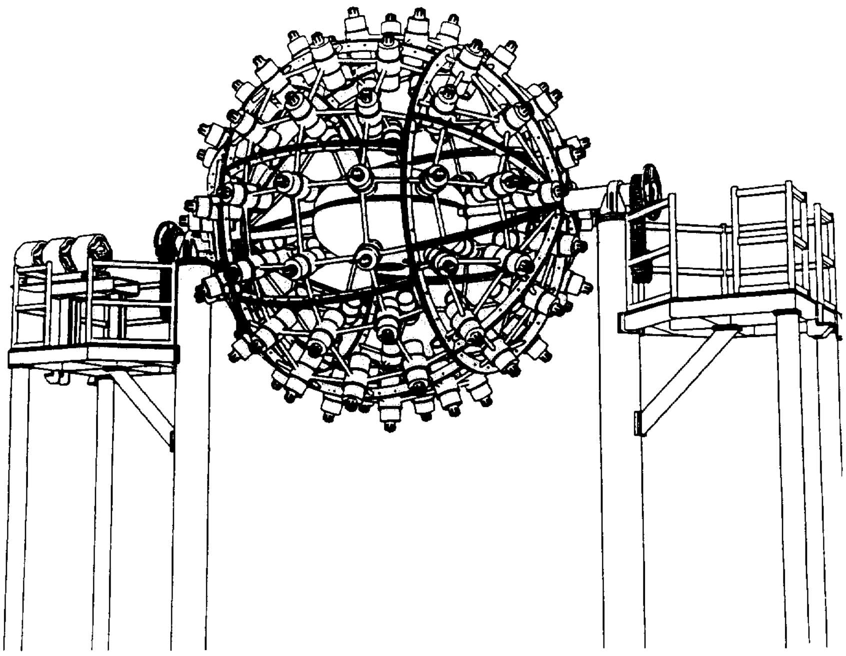

(a)

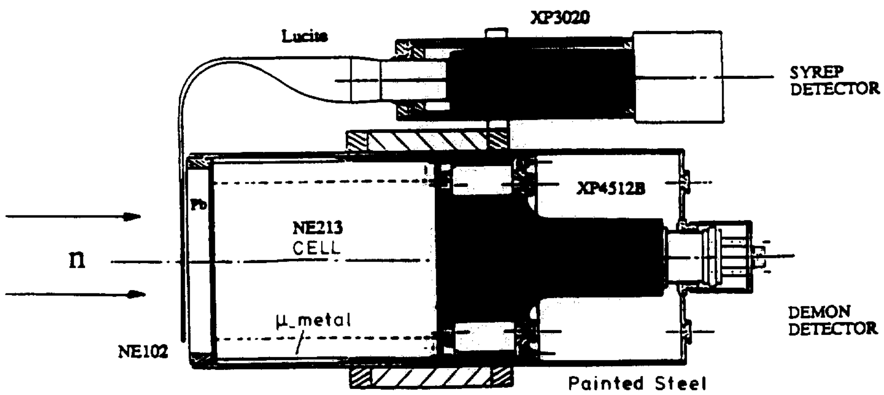

(b)

Fig. 1. (a) CAD view of the mechanical setup of the DEMON detector array (all in aluminium material) in the target hall of Louvain-la-Neuve Cyclotron. (b) Sketch of a DEMON module coupled to a SYREP detector. See text for more details.

(called SYREP), which are 3 mm thick NE102A plastic scintillators coupled to XP3020 phototubes. These detectors can be mounted in front of DEMON cells in anticoincidence with the associated neutron detector. Fig. 1b shows a schematic drawing of a DEMON module and the attached SYREP detector.

The DEMON modules have been tested using radioactive sources. Some of the results concerning the effects of pulse currents on the behaviour of the large area photomultipliers are presented in Section 2. The high light output of the large volume NE213 scintillator will be discussed and an energy calibration method using cosmic rays is described in Section 3. Some modules have been tested using monoenergetic neutron beams in order to determine the neutron detection efficiency as a function of the incident neutron energy. The influence of the cross talk between adjacent cells and of the SYREP–DEMON coupling on the efficiency is analysed in Section 4. Monte Carlo simulations of the response functions are compared with the experimental data. The conclusions are summarized in Section 5.

2. Comparative study of the neutron detection modules

Each DEMON cell is a cylinder of 16 cm diameter and 20 cm length, designed with an expansion volume and painted with TiO_2 white reflector. A cell contains 4 liters of liquid scintillator NE213 in an aluminium container having a 6.35 mm thick front entrance and a 21.5 mm thick wall. The cell back window of 10 mm thick glass is directly coupled to a 130 mm diameter XP4512B magnetically shielded fast PM. The tube is supplied with a grounded anode divider which, for the recommended supply voltage (V) of 1700 V, typically ensures a gain of 5.0×10^6. The standard anode pulse rise time is 2.1 ns, the intrinsic PM pulse duration at half maximum is 3 ns and the signal transit time is (49 ± 1.3) ns for full cathode illumination. The manufacturer gives a slope of log(gain)/log(supply voltage) = 7.5. A lead absorber of 5 mm thickness is used in front of the cell to lower the exposure to low energy γ-rays, thus allowing a reduction of the n–γ discrimination threshold.

Previous tests of the large area XP4512B tube [1] and a study of the n–γ discrimination technique by digital charge comparison [2] have been published. This discrimination technique compares the intensities of the slow components for the same total integrated charge induced either by the recoil protons or the Compton electrons in the scintillator. Two charge-to-digital converters (QDC) integrate the charge of the total pulse (Q_t) and of the slow component (Q_s). On the two-dimensional plot in Fig. 2a two well separated branches corresponding to incident γ-rays and to neutrons generated by an $^{241}Am^{9}Be$ source are clearly seen. A time gate of 350 ns for Q_t and of 295 ns (delayed by 55 ns) for Q_s were found to optimize the n–γ discrimination for neutron energies up to about 60 MeV. Fig. 2b displays equivalent spectra generated by a 40 MeV monoenergetic neutron beam delivered by the Louvain-la-Neuve Cyclotron. A well separated third branch corresponding to neutron interaction channels in the liquid scintillator such as $^{12}C(n,\alpha)^{9}Be$ and $^{12}C(n,n')3\alpha$ is also observed. The figure shows four projections along vertical cuts (solid straight lines or constant Q_t) of the two-dimensional spectrum. High quality neutron–gamma discrimination is achieved with DEMON detectors. The contribution of neutron interaction channel such as (n,d) is also

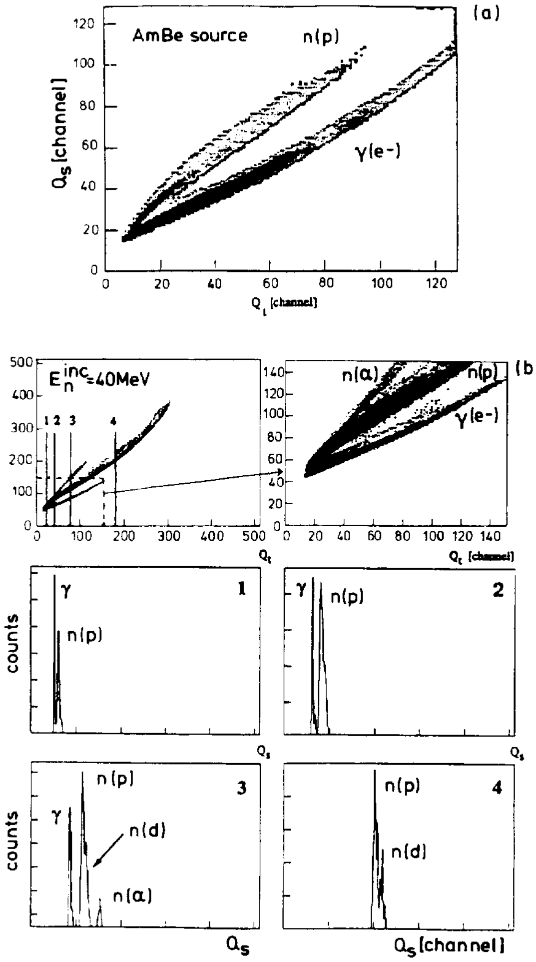

Fig. 2. (a) Two-dimensional plot of slow components Q_s versus total integrated charge Q_t induced by recoil protons (top branch) and Compton electrons (bottom branch) generated by an AmBe source in the NE213 scintillator. Neutron induced events are localized in the upper part; γ-rays and cosmic muon induced signals are in the bottom branch. (b) Similar spectra induced by a 40 MeV monoenergetic neutron beam; the third observed branch corresponds to $^{12}C(n,x\alpha)$ interaction channels in the liquid scintillator. Four monodimensional spectra ((b)1,2,3,4) correspond to the projection of the two-dimensional plot along vertical cuts (Q_t = constant). The neutron contributions from (n,p), (n,d) and (n,α) processes are shown.

shown. Multiway GAN'ELEC modules in CAMAC standard were used: the QDC1612F charge-to-digital converter for the analog signal integration, the FCC8 constant fraction discriminator to generate the logical signal and the TDC812F time-to-digital converter for time-of-flight measurements, the data acquisition being in VME standard. An "inhibit" condition has been applied to the data flow during the handling of each event, thus preventing superposition of consecutive hits. The acquisition rate was limited to $\approx 10^3$ events per second in order to minimize the acquisition dead time and to avoid non-linearity in the energy response.

2.1. Standard light output calibration

The light output LI is usually expressed in MeV *equivalent-electron* (MeVee), which allows a comparison irrespective of the nature of the detected particle. With DEMON, the energies of neutrons are measured by time-of-flight. Nevertheless, an energy calibration in "light units" MeVee of the NE213 scintillation cell is highly desirable. It allows definition of the energy threshold (about 0.1 MeVee) for n–γ discrimination needed to determine the integral neutron detection efficiency. The γ-rays and the cosmic muons are localized on the electron branch in the two-dimensional plot Q_t–Q_s of pulse charge integration. Their light output is presumed to be proportional to the energy deposition of the recoil electrons or muons. For heavier particles the light output also depends on the mass of the particles. The behaviour of the DEMON modules has been studied using the light output corresponding to the Compton edge of the γ-ray sources ^{22}Na, ^{137}Cs and AmBe; the response to cosmic muons was also investigated (see Section 3). In addition, the ^{228}Th radioactivity present in the glass material of the modules was exploited. The γ-ray energies, E_γ, and the corresponding Compton edge values, E_C, are listed in Table 1; their light output values are labeled L1, L2, L3, L4, L5, respectively.

2.2. Module relative gain and linearity

With the standard light output calibration, the relative gain and linearity of DEMON modules were studied. This comparative analysis used 50 detectors randomly chosen. Assuming identical NE213 scintillator cells and voltage dividers, deviations should be mainly due to differences of the XP4512B photomultipliers. Fig. 3 presents the experimental charge-to-light output ratio Q_t/L as a function of the supply voltage

Table 1
Standard γ-ray sources used for the light output calibration LI of DEMON cells. Energies E_γ and the corresponding Compton edge E_C values are listed

LI	Source	E_γ [MeV]	E_C [MeVee]
1	^{22}Na	0.511	0.341
2	^{137}Cs	0.662	0.478
3	^{22}Na	1.274	1.061
4	^{228}Th	2.615	2.382
5	^{241}Am^{9}Be	4.440	4.198

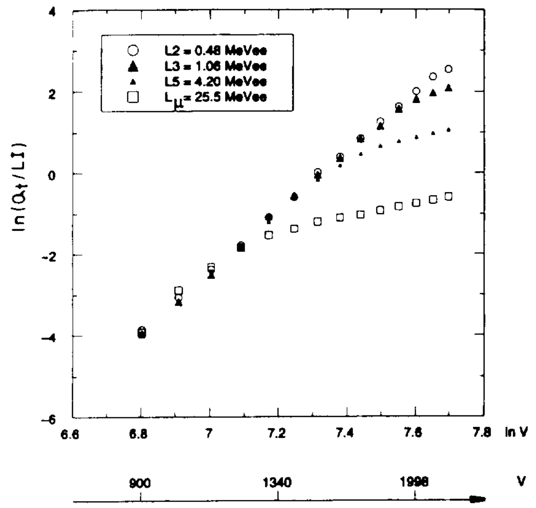

Fig. 3. The logarithm of the total integrated charge Q_t normalised to the light output LI (see Table 1) induced in the scintillator cell versus the logarithm of the supply voltage of a DEMON module.

V of a DEMON module. The common linear response zone of all the tested PM (up to ln $V = 7.1$ or $V \sim 1200$ V) could be described by the relation:

$$Q_t/L \propto V^n. \quad (1)$$

where n is related to the number of amplification stages of the photomultiplier [3]; $n \sim 7.5$ was found as given by the manufacturer. Above 1200 V the response functions deviate from relation (1) and Q_t/L starts to saturate. For high light outputs, saturation already occurs at low voltages and thus the photomultipliers are operating in a non-linear regime. The non-linear response is illustrated in Fig. 4a, where the calibration curves (Q_t versus L) are plotted for some typical DEMON modules operating at a constant $V =$ 1700 V. The tested tubes differ in gain and linearity. The Q_t values at saturation do not correspond to the same value of L. These features seem to depend on individual characteristics of the XP4512B such as amplification properties or quantum efficiency B.

However, once the supply voltages V'_i of the modules were adjusted to obtain the same Q'_t for a given output L (L2 = 0.478 MeVee), the calibration curves shown in Fig. 4b are similar. Thus the $Q_t/L = f(V)$ functions can, in practice, be homogenized by an individual voltage adjustment.

One can correlate the linearity (l) of the PM response functions to the overall gain (G). We define the linearity as:

$$l = Q_t(\mathrm{L5})/Q''_t(\mathrm{L5}), \quad (2)$$

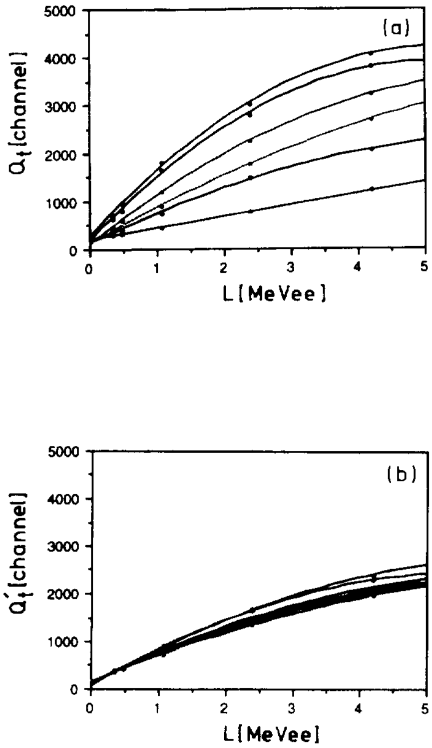

Fig. 4. (a) Light output response of several DEMON modules at a constant supply voltage $V = 1700$ V. The experimental data (black circles) were fitted by polynomial second-order curves. (b) Light output response after adjusting the supply voltages V'_i in order to obtain the same integrated charge Q'_t at a given value of the light output (that induced by ^{137}Cs γ-rays).

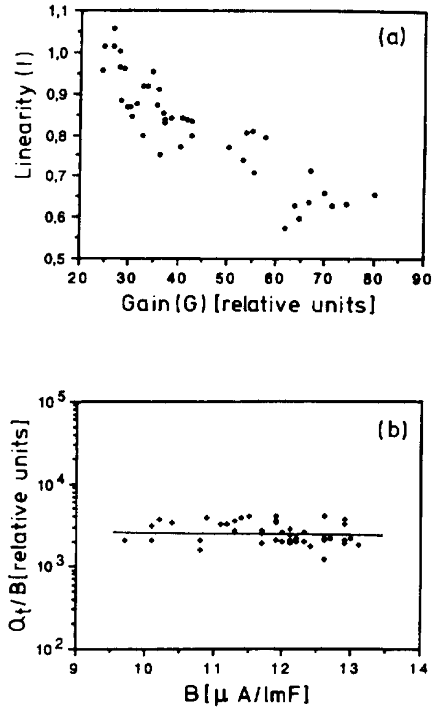

Fig. 5. (a) Linearity of light output L5 versus gain at L2 (the chosen reference light output) for different modules at constant photomultiplier voltage $V = 1700$ V (see Table 1). (b) The gain ∝ Q_t/B plotted in a log scale versus the cathode sensitivity B for the tested modules, under the conditions in (a); the solid line corresponds to the best linear fit.

where $Q_t(\mathrm{L5})$ is the measured value corresponding to the AmBe γ-ray output light and $Q''_t(\mathrm{L5})$ is the calculated total charge obtained by extrapolating at L5 the straight line defined by the two points $Q_t(\mathrm{L2})$ and $Q_t(\mathrm{L3})$ for each module "i". The amplification factor of a PM is defined as the ratio of the integrated anode charge, Q_t, to the corresponding photocathode charge q_c. The latter is proportional to the product of the scintillator light output L and of the cathode luminous sensitivity (or quantum efficiency) B, thus $q_c \propto LB$ and $G \propto Q_t(L)/LB$. Expressed in relative units, $G \propto Q_t(\mathrm{L2})/B$ for constant light output $L = \mathrm{L2}$. Eq. (1) describes this gain for a constant B (one photomultiplier) but for different light outputs. Fig. 5a presents the linearity versus gain at $L = \mathrm{L2}$ for different modules "i" at $V = 1700$ V. The quantum efficiencies B_i supplied by the manufacturer were used. The two quantities appear to be correlated: the higher the gain of a phototube, the worse is its linearity.

What makes the phototubes so different? There are of course the manufacturing parameters: the luminosity sensitivity of the photocathode (B) and its homogeneity, the intrinsic photomultiplier amplification and the charge collection performances at the different amplification stages. Usually, one has access only to the parameter B.

The blue cathode sensitivities for these tubes vary by up to 20% around a mean value of about 11 μA/lmF ("F" as Filtered). We focus the discussion on a fixed value $L_c = \mathrm{L5}$ (the light output of the AmBe γ-ray source). Under such conditions the overall gain G_i of the different photomultipliers at $V_c = 1700$ V can be expressed as:

$$G_i \propto V_c^{n_i} \propto Q_{t,i}(\mathrm{L5})/B_i. \qquad (1')$$

Fig. 5b displays the relative gains (G_i) of the tested modules (i) as a function of the B_i values supplied by the manufacturer. The G_i are weakly dependent on B_i but remained highly dispersed. This dispersion can be linked to differences in the saturation observed at high voltage, which is related to differences in the secondary electron emitting surfaces of the PM dynodes and to space charge effects due to high anodic currents (which can reach up to several tens of mA per pulse).

3. Cosmic rays and monoenergetic neutron and proton beams used for the calibration of the NE213 scintillator at high light outputs

High light outputs of 40 MeVee are expected to be induced in the NE213 cell by intermediate energy beams. An understanding of the high light output response is required to compare the data with Monte Carlo simulations and to choose a suitable amplification scale in the Q_t–Q_s plot. γ-Ray sources of high photon energies are not available and the calibration at low photon energies cannot be extrapolated reliably. This is shown in Fig. 6a by the dashed straight line and parabola fitting the data of standard γ-ray sources. Fortunately, cosmic rays can be exploited because they are efficiently detected in such large size scintillators.

Very approximately, at sea level, about 75% of cosmic rays are energetic muons of both charges. Most of them are minimum ionizing particles (MIPs) having a rest mass of 105.66 MeV and differential momentum spectra centered around 400 MeV/c, where c is the velocity of light. The angular distribution with respect to the zenith angle Θ is proportional to $\cos^2 \Theta$.

The muon path distribution through a DEMON cell (r in mm) has been simulated for horizontal and vertical positions (Figs. 7a and 7a′, respectively). The good agreement with the experimental shapes of the Q_t spectra shown in Fig. 7b,b′ confirm our calculations. Knowing the NE213 scintillator composition and making use of the energy loss of muons in hydrogen and carbon elements [4,5], their energy deposition as MIPs in the cells has been simulated in both positions (horizontal and vertical). The average energy loss of the cosmic muons in the horizontal and vertical position of our scintillator cells is 25.5 and 33.7 MeV, respectively. The solid line in Fig. 6a represents the calibration curve calculated using the muon values and those from the γ-ray sources (the bottom five open circles). The large open circle at 15 MeVee in Fig. 6a lies on the solid curve (thus confirming our calibration method). The γ-ray emitted by the 15.1 MeV excited state of ^{12}C was obtained in the $^{12}C(p,p')^{12}C^*$ reaction with a 35 MeV proton beam on a thick carbon target. At 15.1 MeV, the photon cross section in the NE213 scintillator cell is equally shared between Compton scattering and pair production [4]. With this assumption the corresponding 15 MeVee value of the light output has been calculated, neglecting the escape of annihilation photons from our large volume detector. Fig. 6b displays the light output for γ-rays (six open

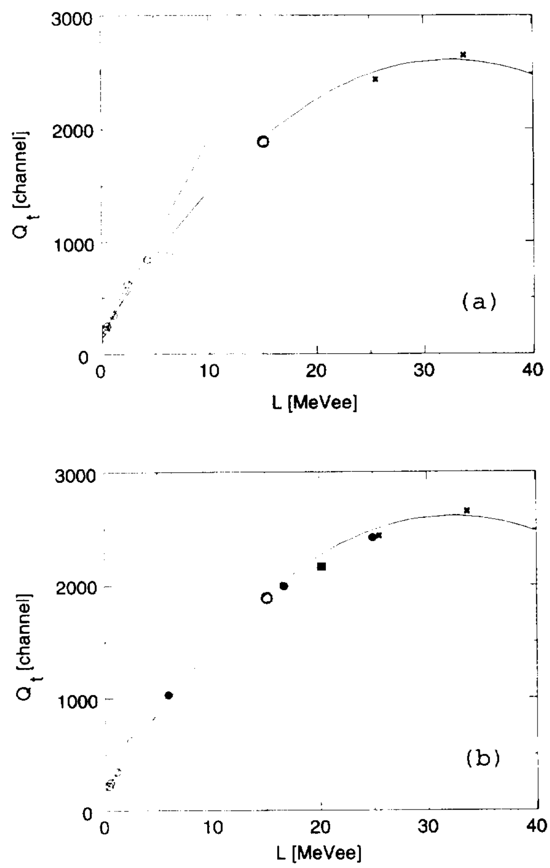

Fig. 6. Light output calibration using muon cosmic rays. (a) The total pulse integrated charge versus the light output value. The five open circles correspond to Compton edge values of the γ-rays supplied by standard radioactive sources (fitted by the dashed straight line and the dotted parabola). The two crosses correspond to light outputs induced by cosmic muons for horizontal and vertical cell positions (see Fig. 7). These seven points were fitted by the solid parabola. The large open circle is from 15.1 MeV γ-rays induced by 35 MeV protons $^{12}C(p,p'\gamma)$. (b) Light outputs induced by neutron (solid circles) and proton incident beams (solid squares) added to Fig. 6a and calculated by means of the parametrization in Ref. [8].

circles), cosmic muons (two crosses), neutrons (three solid circles) and protons (one solid square). The data points for neutrons and protons were obtained by directly irradiating a DEMON cell with (i) neutrons of 10 MeV (the edge point of the neutron spectrum from an AmBe source [6]), (ii) 23.4 and 33.4 MeV monoenergetic neutron beams [7] and (iii) a 27.6 MeV proton beam. The experiments were performed at the LLN Cyclotron. The light outputs for neutrons and protons in the NE213 scintillator were computed using

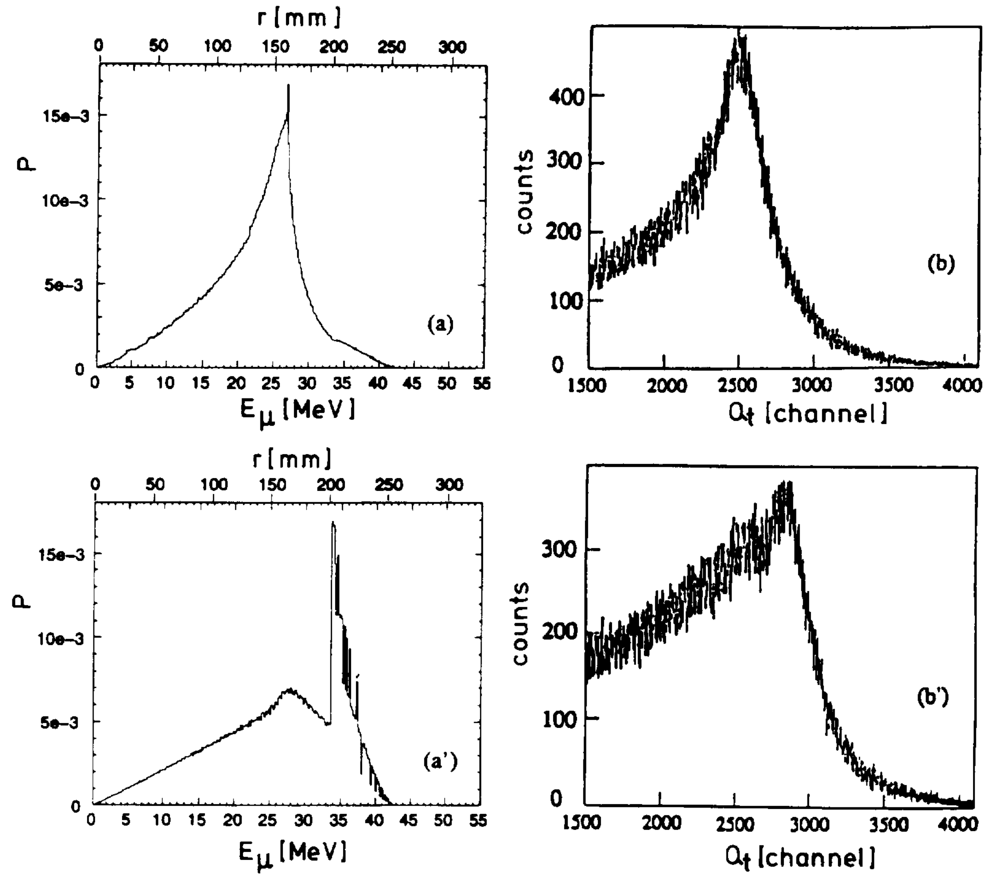

Fig. 7. Energy loss spectra of cosmic muons for horizontal (a,b) and vertical (a',b') positions of the cylindrical scintillator cell. (a,a') From the computed distribution P vs. the distance r (mm) traversed by the muons inside the scintillator for the two extreme positions, respectively, the muon energy depositions were calculated assuming $(\mathrm{d}E/\mathrm{d}x)_{\mu} = 1.675$ MeV/cm in NE213. (b,b') The corresponding experimental light output distributions (expanded).

the parametrization of Madey et al. [8]. A good overall agreement is obtained.

4. Neutron detection efficiency of the DEMON cell

The DEMON detector array has to measure: cross sections, absolute multiplicities, energy and angular distribution of neutrons emitted in heavy ion induced reactions. For a reliable analysis, one has to discriminate the neutrons from other events to which NE213 is sensitive, i.e. γ-rays and energetic light charged particles, mainly protons. In order to determine the intrinsic efficiency of the scintillator cell for neutrons, the effects of the discrimination method and of the cross talk between adjacent detectors have been studied in detail.

4.1. NE213 scintillator neutron efficiency

The intrinsic efficiency of neutron detection depends on the neutron energy and on the threshold for light output detection. The following procedure was used:

(i) the efficiency was measured at some discrete neutron energies;

(ii) the experimental results were confronted with the available Monte Carlo simulation codes [9,10];

(iii) the results from (i) and (ii) were used to interpolate the efficiency over the entire neutron energy range.

The measurements in the energy interval 8–21 MeV were performed using the monoenergetic neutron beam [7] of the Louvain-la-Neuve Cyclotron. The neutron beams were produced by the ^{7}Li(p,n)^{7}Be reaction ($E_{\mathrm{th}_{\mathrm{r}}} = +1.87$ MeV) at five proton energies 22, 25, 30, 35,45 MeV with 10 μA beam intensities.

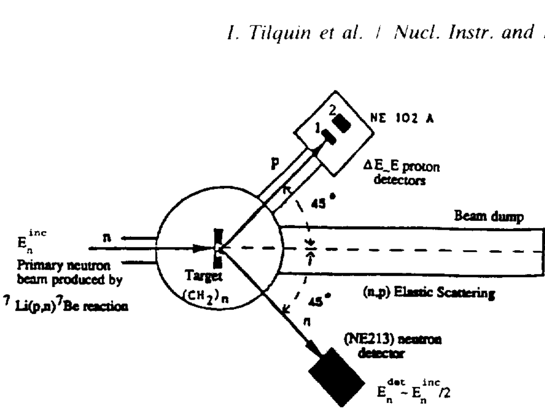

Fig. 8. Experimental setup to measure the intrinsic detection efficiencies of DEMON cells. See text for more details.

The intrinsic efficiency of the DEMON cell was determined by using the correlated charged particle method establishing the ratio of the number of neutrons detected to the number of incident neutrons on a given cell. We exposed a 0.5 mm thick polyethylene $(CH_2)_n$ target to the incident neutron beam in the experimental setup sketched in Fig. 8. In the elastic scattering on hydrogen, each recoil proton ejected at 45° with respect to the direction of the incident beam is correlated with a scattered neutron emitted at 45° to the other side of the beam with half the energy of the incident neutron beam. The protons were identified and counted in a ΔE–E telescope consisting of two NE102 plastic scintillators. The ΔE detector (30 mm in diameter and 0.4–1 mm thick) was used to trigger the acquisition system. The E detector was 40 mm in diameter and 10 mm thick. The intrinsic efficiency of the neutron detector was computed as the ratio of the number of neutrons detected by the DEMON module to the number of protons detected with 100% efficiency by the ΔE–E telescope. The detectors were set at equal distances from the target ($\simeq 1$ m). The 30 mm diameter ΔE proton detector defined the active area in the 160 mm diameter DEMON cell for neutron detection (equal solid angles).

Fig. 9 displays several spectra used to select the

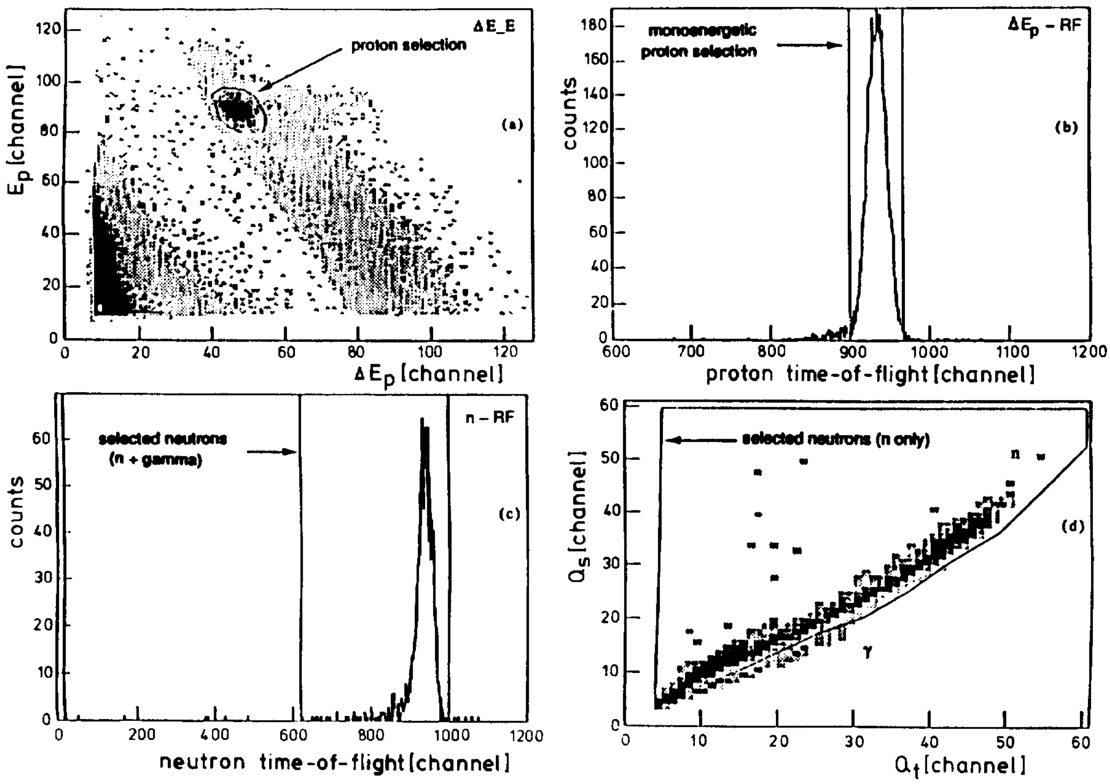

Fig. 9. Illustration of the analysis procedure used to determine the neutron detection efficiency of a DEMON module. (a) The two-dimensional plot ΔE–E for the proton identification. (b) Time-of-flight of the selected protons with respect to the Cyclotron radio frequency (RF): ΔE_p–RF. (c) Time-of-flight of the correlated and elastically scattered neutrons: n–RF. (d) The two-dimensional plot Q_t–Q_s, allowing n–γ discrimination. The remaining γ-rays in this figure are induced by the $^{12}C(n,n'\gamma)$ reaction inside the NE213 scintillator.

scattered monoenergetic protons and the correlated neutrons; successive criteria (i)–(iv) were cumulated:

(i) Fig. 9a: the two-dimensional map ΔE–E (obtained by total pulse charge integration), allowing proton identification. The protons correspond to the scattering on hydrogen and reactions induced on carbon by the 42 MeV neutrons;

(ii) Fig. 9b: the proton time-of-flight with respect to the cyclotron radio frequency (RF) ΔE_p–RF, allowing selection and counting of the monoenergetic protons;

(iii) Fig. 9c: the coincident neutron time-of-flight with respect to the cycloton RF n–RF, allowing the counting of the correlated neutrons detected by the DEMON cell and the evaluation of the random events;

(iv) Fig. 9d: the two-dimensional Q_t–Q_s plot, allowing discrimination between neutrons and γ-rays generated in the liquid scintillator NE213 by $^{12}C(n,n'\gamma)$ interactions.

We note in Fig. 9c that there are a few events in the tail of the n–RF time spectrum: they may be due to incorrect compensation in the constant fraction discriminator. However, their contribution to the efficiency does not exceed 2.5% for the minimum threshold and decreases with increasing threshold. At all bombarding energies, we have subtracted the contribution of the background (n,p) events arising from nuclear reactions on C in the $(CH_2)_n$ target. This contribution was measured by bombarding a pure C target in separate runs. It never exceeded 2% of the n + H elastic events at its maximum at 43.4 MeV, i.e. the highest neutron incident energy.

The last selection (Fig. 9d) on the two-dimensional spectrum Q_t–Q_s allows the computation of two types of intrinsic efficiency ϵ; the first obtained by suppressing the γ-ray events due to $^{12}C(n,n'\gamma)$ interactions inside the NE213 scintillator: efficiency ϵ_n for "*neutron detected as neutron*"; and the second, including also the gamma-rays: efficiency $\epsilon_{n+\gamma}$ for "*neutron detected as neutron and/or gamma*". Note that these γ-rays survive until the Q_t–Q_s selection because they belong to the neutron time-of-flight peak, unlike the other incident γ-rays correlated to the beam, which have shorter time-of-flight. The contribution of $^{12}C(n,n'\gamma)$ events to the total efficiency has thus been measured experimentally. It is about 7% and depends weakly on the neutron energy in our domain of interest. This contribution has to be taken into account in future experiments performed with DEMON when continuous neutron spectra will be recorded and consequently all events of gamma type will be suppressed in the data analysis. The "*operational mode*" efficiency will therefore be ϵ_n; we define N^{inc} the real incident neutron number at a given energy and N^{det} the number of detected neutrons:

$$N^{inc} = N^{det}/\epsilon_n. \quad (3)$$

Monte Carlo simulations of DEMON cell efficiencies were generated using a version of Stanton's code [9] updated by Cecil et al. [10]. This code fully treats the neutron multiple scattering process inside a NE213 scintillator cell. It takes into consideration the interaction channels contributing to the neutron detection: n + p elastic scattering, n + C elastic scattering (non-diffractive and diffractive processes), $^{12}C(n,n'\gamma)$, and ^{12}C(n, charged particle production) such as (n,p), (n,np), (n,α) and (n,n'3α). In Ref. [10] updated inelastic cross sections for neutron induced reactions on carbon and updated light response functions have been introduced. The light output generated by the residual charged particles in the cell is also determined.

Fig. 10 shows the dependence of the efficiency on the threshold at five neutron energies. The simulated and measured intrinsic efficiencies are compared for both cases: $\epsilon_{n+\gamma}$ and ϵ_n, without a normalization factor. The agreement is good at the lowest neutron energy and generally at low thresholds. The observed discrepancies at high neutron energies and high detection thresholds must be associated mainly with a poor description of the n + ^{12}C interactions leading to charged particle production (differential cross sections and angular distributions) in the computer codes. The threshold energies of these reaction channels are higher than 6 MeV, i.e. 6.2 MeV for $^{12}C(n,\alpha)^9Be$ and 13.6 MeV for $^{12}C(n,p)^{12}B$. Measurements of the double differential cross sections for $^{12}C(n,px)$, (n,d*x*), (n,t*x*) and (n,α*x*) reactions are presently underway at Louvain-la-Neuve. These data could then be included in the computer codes. At low detection threshold, the efficiency dependence is highly sensitive to: (i) the energy calibration in the low pulse height region of the Q_t experimental spectra; (ii) the quality of the experimental n–γ discrimination; and (iii) the low light output estimate of the computer code. At high incident neutron energies the computer code may also underestimate the processes leading to low light output.

Volume limitations may also play a role. Fig. 11a compares the ϵ_n results at 9.4 MeV as a function of threshold for a centrally and eccentrically irradiated cell. When the detector front surface is irradiated off center, we obtain a relative decrease of 5% of the measured efficiencies (twice the decrease obtained with Monte Carlo simulations). The result of experimental tests of ϵ_n for runs with and without the 5 mm thick Pb absorber, at the lowest incident energy of 9.4 MeV, is shown in Fig. 11b. Without shielding, the efficiency increases slightly at the expense of the accuracy of the n–γ discrimination at low light output. The effect of Pb shielding is larger at low detection thresholds and decreases with increasing threshold.

The $\epsilon_{n+\gamma}$ and ϵ_n efficiencies at the lowest threshold

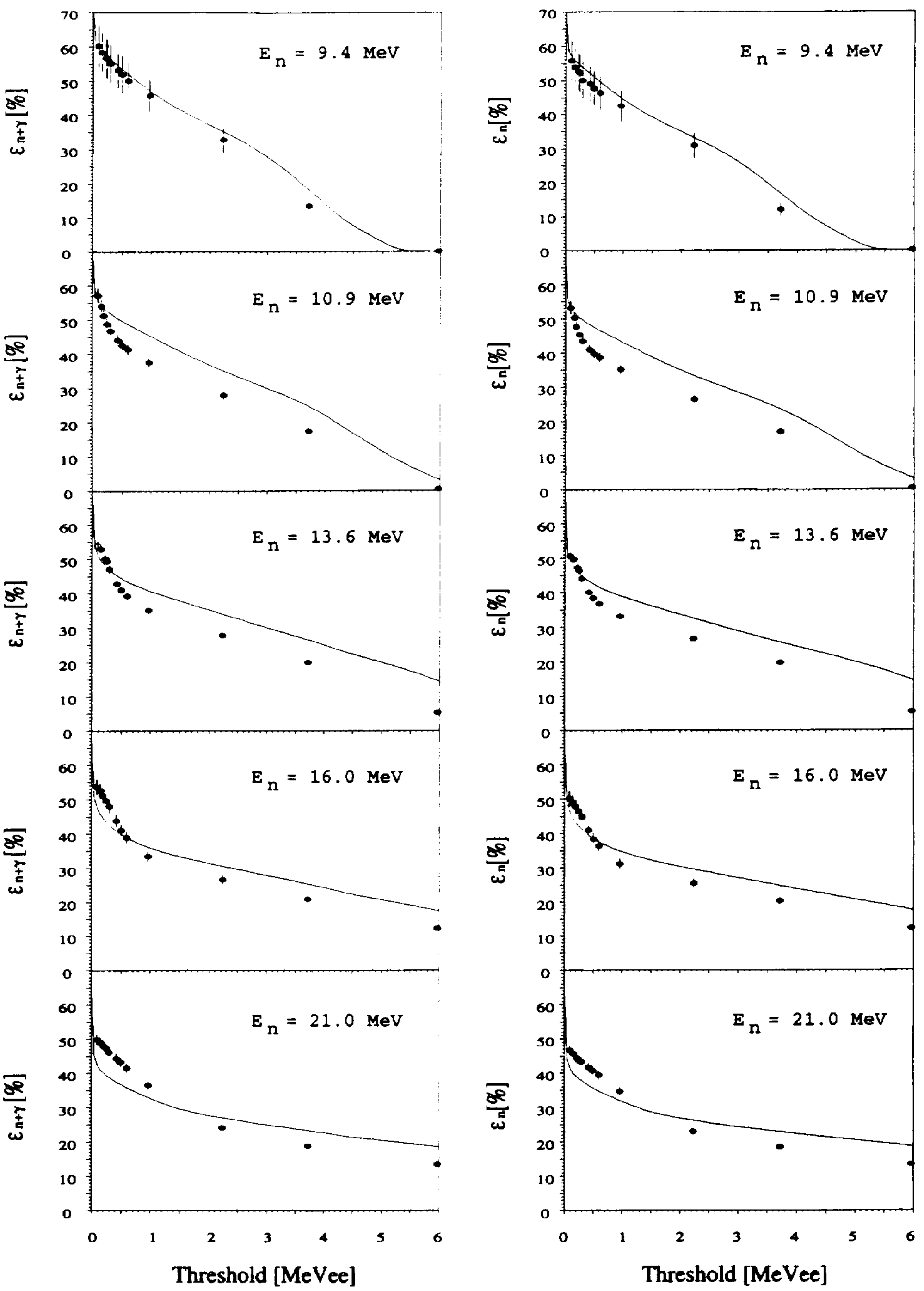

Fig. 10. Neutron intrinsic efficiencies as a function of detection thresholds (MeVee) at $E_n = 9.4$, 10.9, 13.6, 16.0 and 21.0 MeV incident neutron energies. Solid circles denote the experimental values, the curves are Monte Carlo simulations [10]. Efficiencies of both *neutron detected as neutron and/or gamma* $\epsilon_{n+\gamma}$ and *neutron detected as neutron* ϵ_n are plotted. See text for corresponding definitions.

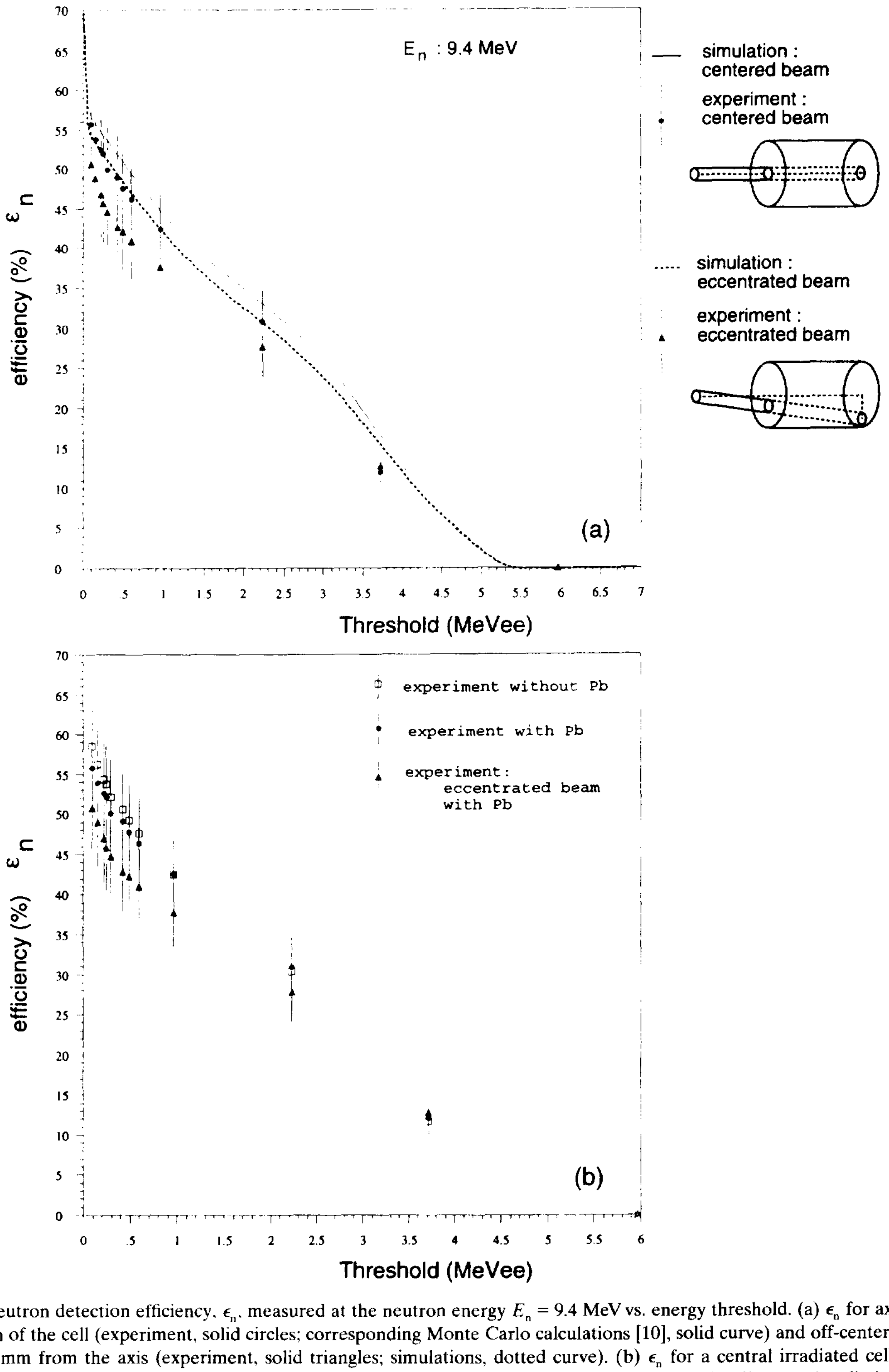

Fig. 11. Neutron detection efficiency, ϵ_n, measured at the neutron energy $E_n = 9.4$ MeV vs. energy threshold. (a) ϵ_n for axial central irradiation of the cell (experiment, solid circles; corresponding Monte Carlo calculations [10], solid curve) and off-center irradiated cell at 60 mm from the axis (experiment, solid triangles; simulations, dotted curve). (b) ϵ_n for a central irradiated cell (shielded with a lead absorber of 5 mm thickness) (solid circles) and without lead absorber (open squares); off-center irradiation data are shown as solid triangles. See text for ϵ_n efficiency definition and details.

(0.1 MeVee) are listed in Table 2 and displayed in Figs. 12a,b. The overall agreement between the simulated and measured values is within 5% and within the experimental errors at the lowest neutron energy. However, the discrepancy between data and simulations increases to 15% at the highest energy. This can be understood as being due to the neglect of neutron interactions in the NE213 scintillator, as already mentioned above, and as concluded also in a recent similar work [12]. The authors of Ref. [12] have measured neutron efficiencies in the same energy range but at a much higher threshold (2 MeVee) for 3.9 liter NE213 scintillator cells used in the SENECA hodoscope, which are similar to ours (4 liters). By integrating our differential efficiency spectra from above 2 MeVee similar experimental results are obtained, as shown in Fig. 12c.

4.2. Neutron transit times in a DEMON cell and the associated dispersions

The peaks in the time-of-flight spectra of Figs. 9b,c have a FWHM of 1.6 ns for protons and 2.0 ns for the correlated neutrons. The width contains contributions from the energy spread of the primary neutron beam (1–1.2 ns), from the proton energy loss in the thick $(CH_2)_n$ target and from kinematical broadening due to the opening angle of the proton telescope ($\sim 4°$) taking into account the dimension of the incident neutron beam spot on the target (3×3 cm^2). For neutrons, one must also include the dispersion of the transit time in the detection cell during the interaction processes with the liquid organic scintillator. The neutron transit time and its dispersion in the detector cell are two important parameters in the neutron energy determination by the time-of-flight technique and for its associated resolving power. The latter can be expressed in the non-relativistic velocity regime in the familiar form:

$$(\Delta E_n^{N.R.}/E_n^{N.R.}) = 2\left[\left(\frac{\Delta t_{tf}}{t_{tf}}\right)^2 + \left(\frac{\Delta l}{l}\right)^2\right]^{1/2}, \quad (4)$$

where Δt_{tf} is the uncertainty in the neutron time-of-flight (t_{tf}) and Δl is the uncertainty in the neutron flight path (l). The timing uncertainty is associated either with electronics (which can be determined experimentally) or with the determination of the exact time at which the burst of neutrons is generated and detected throughout the volume of the detector. Similarly, the length of the flight path is uncertain because the neutron generating target and the neutron detector have finite thickness.

The commonly adopted uncertainty in the neutron flight path corresponds to half the depth of the cell dimension, which is really an overestimation in any

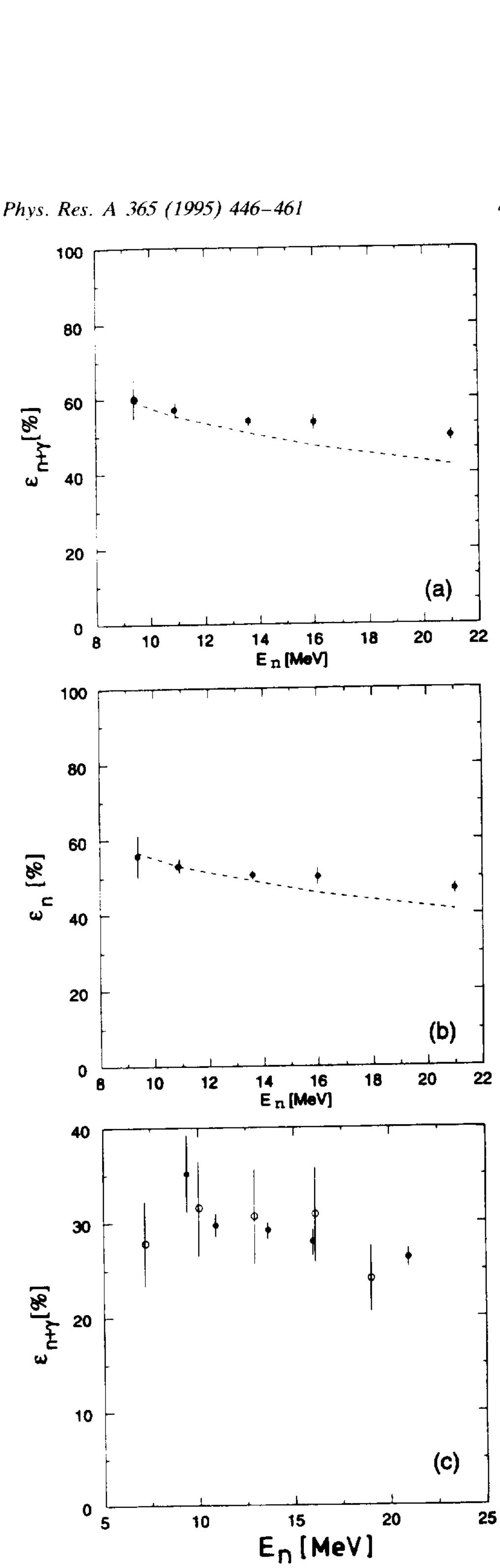

Fig. 12. (a,b) Efficiency of a detector module as a function of the neutron energy, E_n, at the lowest detection threshold 0.1 MeVee. (a) $\epsilon_{n+\gamma}$ and (b) ϵ_n. The solid circles are measured values and the dashed lines are Monte Carlo simulations [10]. The bars account for statistical uncertainties. (c) Present neutron detection efficiencies (solid circles) at 2 MeVee threshold compared with those of Ref. [12] measured in the same neutron energy range (open circles) using 3.9 liter NE213 cells.

case. This is also the reason why, at the expense of the intrinsic detection efficiency, thin detectors are often chosen for neutron time-of-flight energy determination. The Monte Carlo code of Stanton was modified such as to calculate, as a function of the incident neutron energy, the "minimum" distances-of-penetration (x_i) of the neutrons inside the scintillator cell until they interact and produce light output above a given detection threshold. The associated detector response time (t_{di}) is thus defined as the sum of: (i) the transit time (t_{ni}) of the neutron in the scintillator cell along its axis, and (ii) the light propagation time from this interaction point to the PM photocathode through a medium of refractive index $\nu = 1.508$. The "minimum" response time of the scintillator for a given neutron energy E_n is then defined as:

$$t_{di} = t_{ni} + \frac{(L - x_i)}{c}\nu = \frac{L\nu}{c} + \frac{x_i}{c}\left(\sqrt{\frac{M_n c^2}{2E_n}} - \nu\right), \quad (5)$$

where $L = 20$ cm is the depth of the cell, c is the velocity of light and $M_n c^2$ is the neutron mass (939.55 MeV). One sees immediately that t_{di} is at least equal to 1 ns for $x_i = 0$ or independent of x_i for $E_n = (M_n c^2 / 2\nu^2) = 206.58$ MeV, where the light velocity in the cell is equal to the neutron velocity. The expression "minimum" covers the fact that: (i) the neutron in the detector is followed until it interacts giving a light output above the selected detection threshold; (ii) the distance-of-flight of the neutron induced charged particles in the cell is ignored; (iii) the neutron transit time and the light propagation time in the scintillator are estimated along the cylindrical axis (x) of the detector; and (iv) the neutrons are treated only for normal incidence on the detector front window. However, these assumptions are not very restrictive. For example, the departure of the neutron trajectory from the detector axis (or parallel to it) may be associated with cases where the neutron undergoes a multiple scattering process. Monte Carlo simulations using Stanton's code have shown that, in our case, the multiple scattering probability remains below 33% at neutron energies exceeding 5 MeV. This probability drops to 21% at $E_n = 45$ MeV and to 12% at $E_n = 80$ MeV. This can be easily understood recalling that the mean free path (λ) of a high energy neutron inside the NE213 scintillator cell becomes as large (see Table 3) as the cell depth (L): $\lambda(E_n = 45 \text{ MeV}) \sim 20 \text{ cm} = L$.

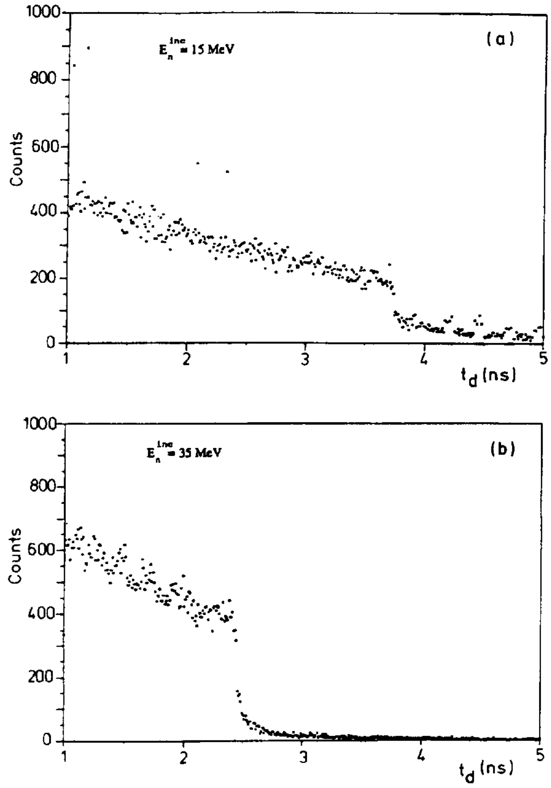

Fig. 13. Typical Monte Carlo simulation of the "minimum" response time t_d of a DEMON module for (a) 15 MeV and (b) 35 MeV neutron energies. See text for more details.

Fig. 13 displays typical Monte Carlo time spectra (t_{di}) in a DEMON cell for 15 and 35 MeV incident neutron energy. From such spectra one defines the mean $\bar{t}_d$ value as $((\sum_{i=1}^{k} t_{di})/k)$, where k is the number of "observed" neutrons. The variance of this distribution can be expressed as $S_{td}^2 = (\sum_{i=1}^{k}(t_{di} - \bar{t}_d)^2)/(k-1)$ and the standard deviation $\sigma_{td} = \sqrt{S_{td}^2}$. σ_{td}

Table 2
Neutron intrinsic detection efficiencies of a single DEMON module, at 0.1 MeVee the lowest experimental threshold, as a function of the neutron energy E_n. Experimental and simulated values [8] are compared. See text for $\epsilon_{n+\gamma}$ and ϵ_n definitions

E_n [MeV]	$\epsilon_{n+\gamma}$ [%]		ϵ_n [%]	
	Exper.	Simul.	Exper.	Simul.
9.4	60.1±5.4	59.3	55.7±5.7	56.8
10.9	57.2±2.0	55.4	53.1±1.9	53.1
13.6	54.0±1.3	50.9	50.6±1.3	49.0
16.0	53.6±2.2	47.3	50.1±2.1	45.8
21.0	49.9±1.6	42.2	46.6±1.5	41.1

Table 3
The neutron mean free path λ as a function of neutron incident energy $\lambda(\text{NE213})=21.3(\text{cm})/(K\sigma_H+\sigma_C)$, with ρ (volumic mass)=0.874 g/cm^3, K=1.213, the (H/C) ratio, σ_H and σ_C the *total* reaction cross sections of neutron interactions with hydrogen and carbon media. Next columns display Monte Carlo simulations of the mean "minimum" distance-of-penetration $\bar{x}$ along the cell axis and the mean response time-of-flight ($\bar{t}_d$) of a DEMON cell and their corresponding standard deviations σ_x and σ_{td}. The last column displays the calculated intrinsic efficiencies at 0.2 MeVee detection threshold [11]

E_n [MeV]	λ [cm]	$\bar{x}$ [cm]	σ_x [cm]	$\bar{t}_d$ [cm]	σ_{td} [ns]	Intrinsic efficiency [%] $\epsilon_{n+\gamma}$
5	7.94	7.07	5.33	3.30	1.83	71.94
10	11.02	7.77	5.55	2.47	1.36	58.18
15	11.58	8.26	5.57	2.30	1.03	58.01
20	12.69	8.48	5.55	2.23	1.08	52.93
25	13.76	9.00	5.66	2.03	0.85	47.39
30	15.41	8.90	5.58	1.86	0.74	43.85
35	17.28	9.00	5.71	1.74	0.59	39.19
40	19.05	9.27	5.70	1.64	0.43	36.31
45	20.64	9.05	5.64	1.55	0.38	34.51
50	22.50	9.36	5.68	1.51	0.34	33.38
55	24.51	9.41	5.72	1.46	0.28	30.88
60	26.64	9.56	5.72	1.43	0.26	28.07
65	28.67	9.36	5.73	1.38	0.24	26.85
70	30.83	9.42	5.76	1.35	0.22	25.56
75	32.31	9.54	5.75	1.33	0.20	24.87
80	33.94	9.47	5.76	1.30	0.17	23.90

defines the simulated time resolution or dispersion of a DEMON detector including all other uncertainties.

Table 3 shows that, for neutron energies ranging from 5 to 80 MeV, $\bar{t}_d$ varies from 3.3 to 1.3 ns and σ_{td} from 1.83 to 0.17 ns. The simulated $\bar{t}_d$ variation may even be expressed analytically as $\ln \bar{t}_d$ [ns] = 1.75 − 0.39 ln E_n [MeV]. From Table 3 one observes that (up to 80 MeV) the neutron's mean "minimum" distance-of-penetration ($\bar{x}$) is practically constant (around 9 cm), while $\bar{t}_d$ and σ_{td} drop rapidly with increasing energy. One clearly sees that the σ_x values are smaller than the commonly adopted distance-of-flight uncertainty, i.e. the half depth of the cell.

In conclusion, with an iterative procedure, it is possible to correct the external time-of-flight of the incident neutron for its transit time inside the scintillator [11]. The total time-of-flight resolution and consequently the associated resolving power for high energy neutrons are less affected by the large size of the scintillator cell than expected.

4.3. Detection cross talk probabilities

It is generally admitted that the cross talk between two adjacent neutron detectors is important when their relative spatial separation is small compared to the intrinsic size of a detector. Neglecting the cross talk effect results in an overestimate of the intrinsic neutron efficiency of large cells; it also causes an artificial increase in the rate of high-fold coincidences.

In the configuration of the DEMON setup at Louvain-la-Neuve, the shortest distance between two adjacent modules is about three times the mean dimension of the NE213 scintillator cell (the relative angles with respect to the target position set at 1.75 m distance are greater than 20°). In this geometry, we have exposed a DEMON module M_0 to a direct neutron beam of 37 MeV. The single events (N_{0S}^{det}) detected as neutrons were recorded at different thresholds. Coincident events (N_{1C}^{det}) identified as neutrons by another DEMON module M_1 were recorded. The latter was well shielded against the incident beam (10^{-4} shielding leakage). The "neutron–neutron" cross talk probability (P_{10}^{nn}) of module M_1 relative to module M_0 is expressed as:

$$P_{10}^{\text{nn}} = N_{1C}^{\text{det}} / N_{0S}^{\text{det}}. \tag{6}$$

For example, at detection thresholds of 0.34 MeVee (M_0) and 0.04 MeVee (M_1), the experimental cross talk probability was found to be $P_{10}^{\text{nn}}\text{exp.} = (1.06 \pm 0.08) \times 10^{-3}$. The result of the Monte Carlo simulation [8], $P_{10}^{\text{nn}}\text{simul.} = (1.22 \pm 0.09) \times 10^{-3}$, is in good agreement with the experiment. Taking into account only the four first neighbours in the present configuration, the real incident number of neutrons in module M_0 using Eq. (3) is:

$$N_{0S}^{\text{inc}} \simeq (N_{0S}^{\text{det}}/\epsilon_n)(1 - \sum_{i=1}^{4} P^{\text{nn}}{}_{0i}) \simeq (N^{\text{det}}{}_{0S}/\epsilon_n)(1 - 0.004). \tag{7}$$

The effect of cross talk, at the specified neutron energy and detection threshold, increases the intrinsic neutron efficiency $\epsilon_n = 0.2$ by $0.004\epsilon_n$, half a percent of the ϵ_n value. The contributions of farthest neighbours to the cross talk are much lower and have been neglected.

At low incident energies the neutron efficiency is higher, typically 0.5, but the escape probability is smaller, and consequently the cross talk effects decrease. We may conclude that, in the Louvain-la-Neuve setup of DEMON, the n–n cross talk contribution to the efficiency is less than 1% and can therefore be neglected in most cases.

The two-fold coincidence probability of an equivalent experimental setup ($N = 96$ detectors, $\Omega_{total} = 5 \times 10^{-2} \times 4\pi$) for events of a neutron multiplicity $m = 10$ is 5.82×10^{-2}, which is 50 times greater than P_{10}^{nn}. However, this factor will decrease for lower neutron multiplicity and for very low multiplicities the cross talk may impose an experimental limit.

The data processing method allowed us to determine, besides the "neutron–neutron" cross talk probability (P_{10}^{nn}) of module M_1 relative to module M_0, three other types of cross talk contributions: (i) the neutron seen as a neutron by module M_0 and as a γ-ray by module M_1 as a result of $^{12}C(n,n'\gamma)$ interactions in the detector ($P_{10}^{\gamma n}$); (ii) the neutron seen as a γ-ray in M_0, but as a neutron in M_1 ($P_{10}^{n\gamma}$); and (iii) the neutron seen as a γ-ray in both modules ($P_{10}^{\gamma\gamma}$). Figs. 14a–14d show these measured probabilities plotted versus the detection thresholds in module M_1, the threshold in module M_0 being fixed at 0.34 MeVee. The simulations [10] are plotted as solid lines. They are in good agreement with the experimental neutron–neutron cross talk probabilities, while major discrepancies appear for the other three cases involving γ-rays; the latter are of little importance to the absolute efficiency. Our results indicate that some cross sections in the codes are known with insufficient precision or neglected.

4.4. SYREP–DEMON coupling

Up to 24 DEMON cells are equipped with the rejection system for energetic light charged particles SYREP. A SYREP detector consists of: (i) a 3 mm thick NE102 plastic scintillator covering the entrance

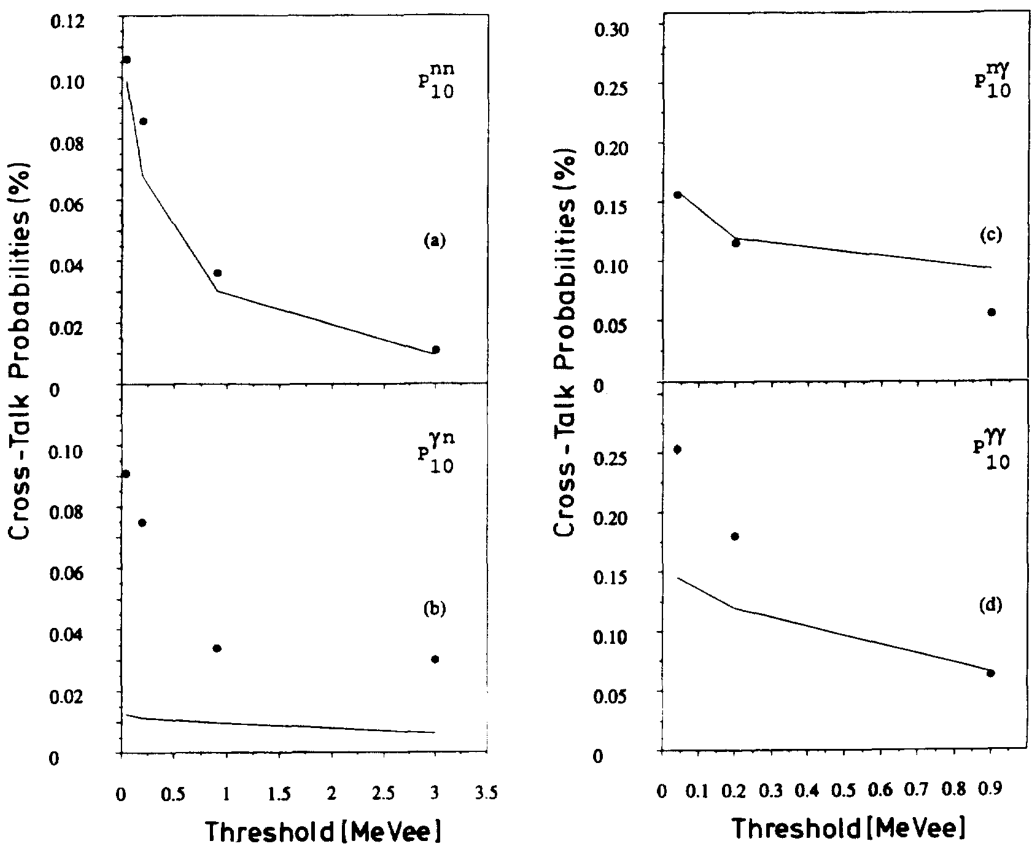

Fig. 14. (a)–(d) Cross talk probability as a function of the detection threshold of detector M_1 at 37 MeV neutron incident energy. The solid circles denote measured values, the full lines are Monte Carlo calculations [10]. See text for probability definitions.

surface of a DEMON cell; (ii) a curved lucite light guide which bends the scintillation light by 90° (compact mechanical assembly with the DEMON module); and (iii) a fast XP3020 photomultiplier (see Fig. 1b). The plastic scintillator has an octagonal shape in order to ensure optimal light collection. By using it as a ΔE transmission detector in a setup with a second thick plastic scintillator of E type, its homogeneity was checked with well collimated proton beams of 21, 40 and 65 MeV. At all three proton energies we found a 100% efficiency, within statistical errors, irrespective of the irradiated zone. Variation for the light collection as a function of the beam impact position on its surface was 30%.

Coupled to a DEMON cell in coincidence mode, SYREP was tested in a proton beam of 50 MeV and a 100% efficiency was found with respect to the DEMON module. In a similar configuration we have tested the SYREP–DEMON coupling in neutron beams of 23.4 and 33.4 MeV and found for SYREP neutron detection efficiencies of 0.27 and 0.39% with respect to the DEMON cell. In the anticoincidence operating mode, SYREP will reject energetic protons with 100% efficiency, but one might also reject up to about 0.4% of the incident neutrons with energies up to 33.4 MeV. This remains a negligible percentage. A SYREP detection efficiency of 0.26% relative to the DEMON cell efficiency was measured for 4.44 MeV γ-rays.

5. Conclusions

The modules of the neutron multidetector DEMON are large size NE213 scintillator cells equipped with large diameter XP4512B Philips photomultipliers. Tests of several modules revealed specific characteristics which have to be taken into account. A comparative study of the modules showed saturation effects in the integrated charge from the photomultiplier. This occurred mainly at high light outputs of the scintillator and at high supply voltages (> 1200 V), affecting both the amplification gain and the linearity. A calibration method for the light response up to 40 MeVee was developed by means of the energy loss of cosmic muons in the liquid scintillator. The neutron detection efficiency was measured in the energy range 8–21 MeV with different detection thresholds, the lowest being 100 KeVee. The experimental uncertainties remained below 12% and were typically less than 5%. The relative weight of the $^{12}C(n,n'\gamma)$ interaction channel was determined experimentally. Its contribution to the total neutron efficiency, weakly dependent on the energy, reaches about 7% at 100 KeVee threshold. For neutron energies lower than 15 MeV and low detection thresholds Monte Carlo simulations account well for the neutron detection efficiencies, but they underestimate the data at higher energies by more than 15%. Neutron–neutron cross talk effects in a given module, summed over all the adjacent modules, were found to be less than half a percent of its intrinsic efficiency. These effects can be neglected in the Louvain-la-Neuve configuration of DEMON. The light charged particle rejection system associated with a DEMON module is 100% efficient, with a negligibly small influence on its neutron detection efficiency.

Acknowledgements

The authors are indebted to the crew of the Louvain-la-Neuve Cyclotron for the excellent running of the machine and Dr. W. Galster for careful reading of the manuscript. They wish to thank also the electronic and mechanical workshops of the I.P.N. and the LPC of Caen for their excellent support of this work.

References

[1] M. Moszynski, G.J. Costa, G. Guillaume, B. Heusch, A. Huck and S. Mouatassim, Nucl. Instr. and Meth. A 307 (1991) 97.
[2] M. Moszynski, G. Bizard, G.J. Costa, D. Durand, Y. El Masri, G. Guillaume, F. Hanappe, B. Heusch, A. Huck, J. Peter, Ch. Ring and B. Tamain, Nucl. Instr. and Meth. A 317 (1992) 262.
[3] W.R. Leo, Techniques for Nuclear and Particle Physics Experiments (Springer, Berlin, 1987).
[4] Particle Data Group Review of Particle Properties, Phys. Lett. B 239 (1990) 1.
[5] W. Lohmann, R. Kopp and R. Voss, CERN 85-03, Experimental Physics Division (March 1985).
[6] E.A. Lorch, Int. J. Appl. Radiat. Isot. 24 (1973) 585.
[7] A. Bol, P. Leleux, P. Lipnik, P. Macq and A. Ninane, Nucl. Instr. and Meth. 214 (1983) 169.
[8] R. Madey, F.M. Waterman, A.R. Baldwin, J. Knudson, J.D. Carlson and J. Rapaport, Nucl. Instr. and Meth. 151 (1978) 445.
[9] N.R. Stanton, COO-1545-92 (February 1971).
[10] R.A. Cecil, B.D. Anderson and R. Madey, Nucl. Instr. and Meth. 161 (1979) 439.
[11] A. Adachour, Diplome d'Etudes Approfondies en Physique, Université Catholique de Louvain, Belgium (1990), unpublished.
[12] G. v. Edel, O. Selke, C. Pöch, F. Smend and M. Schumacher, Nucl. Instr. and Meth. A 332 (1993) 224.